Universidade de São Paulo

Kauê Lima Curvelo da Silva

Azopolymers surface structuring by femtosecond pulses

São Carlos
04 de Dezembro de 2020

Kauê Lima Curvelo da Silva

Azopolymers surface structuring by femtosecond pulses

Trabalho de Conclusão de Curso – Monografia apresentado ao curso de graduação em Física na habilitação Óptica-Fotônica no Instituto de Física de São Carlos da Universidade de São Paulo, como requisito para obtenção do título de Bacharel em Física.

Orientador: Prof. Dr. Cleber Renato Mendonça

São Carlos
04 de Dezembro de 2020

Table of Contents

1) Abstract 2

2) Introduction 2

3) Fundamental Aspects 3

4) Experimental 10

5) Results 11

6) Conclusions 17

7) References 17

1) Abstract

The use of femtosecond laser to modify the surface of polymeric materials has received great attention in the last decade, due to the possibilities of tailoring the material's properties yielding technological applications. This work presents the microfabrication of an azopolymer by using femtosecond laser pulses, aiming at the control of surface wettability. To begin with, a concise introduction to nonlinear optics and ultrashort pulses theory is given, as well as the main theoretical model for wettability in rough surfaces. Secondly, the experimental basis and setups for femtosecond laser microfabrication are described, alongside with the most important features of the azopolymer used. To conclude, the results of microfabrication characterization and the surface wettability control are presented. By properly patterning the polymeric surface structure, we were able to increase the surface hydrophilicity, decreasing the water contact angle by about 15 degrees.

2) Introduction

This work aims to structure azopolymers surface via femtosecond laser pulses to control its wettability. The azopolymer of choice is the TFEMA-DR13, a copolymer synthetized through conventional radical polymerization of 2,2,2 trifluorethyl methacrylate (TFEMA) with 40 -[N-ethyl-N-(2,methacryloxy-ethyl)]amine-4-nitro-azobenzene (DR13MA), which presents high thermal and mechanical stability [1].

The control and optimization of surface wettability have been attracting considerable attention in the last few years due to its wide range of applications, including anti-adherent and self-cleaning devices [2], [3], micro/nano-fluidics [4], cell proliferation [5], anti-fogging [2], and bio-medical devices engineering [6]. Some of these applications require superhydrophobic surfaces, on which water droplets cannot stick and instead slide easily, as in leaves of Lotus flowers, whilst others demand superwetting (super hydrophilic) surfaces on which water spreads completely, as opposed to forming droplets. A facile way to express hydrophobicity and hydrophilicity is by the water contact angle (WCA) of droplets resting on the surface. The WCA is the angle between the liquid-solid interface and the tangent line of the curve at the contact point of the solid/liquid/gas. Then superhydrophobic surfaces are characterized by WCA greater than 150° and super hydrophilic are those with WCA lower than 10°.

Numerous studies have been conducted on the conditions for surface wettability [7], asserting as having a prominent role in the combination of surface chemistry and morphology. In this direction, several approaches have been used to modify the surface of different materials. For polymers specifically, techniques such as plasma treatment [8], chemical treatment [9], and electron beam irradiation [10], had been employed. In this context, femtosecond lasers (fs-laser) micromachining is a promising method for modifying surface wettability, once it allows the microfabrication of periodic patterns with high resolution (sub-micron), thanks to the nonlinear light matter interaction; at nonlinear absorption regime the material excitation is localized and only a minimal heat-affected zone surrounding the laser spot is generated, besides others advantages such as control of patterns size and processing time [11].

Thus, characterization of the optical properties and microfabrication conditions on the TFEMA-DR13 copolymer, as well as the microfabrication setup assembled, are presented. Furthermore, a microstructuring pattern produced on the polymer surface is described, and its influence on the wettability properties of TFEMA-DR13 studied.

3) Fundamental Aspects

3.1) Nonlinear optics

In fs-laser micromachining, the light-matter interaction is governed by nonlinear optical processes. This basically means that the perturbation on the matter due to radiation no longer can be expressed as the usual, linear, polarization:

$$\boldsymbol{P} = \varepsilon_0 \chi \boldsymbol{E} \tag{1}$$

but as a nonlinear dependence with the radiation field:

$$\boldsymbol{P} = \varepsilon_0 \chi^{(1)} \boldsymbol{E} + \varepsilon_0 \chi^{(2)} \colon \boldsymbol{E}^{\boldsymbol{2}} + \varepsilon_0 \chi^{(3)} \therefore \boldsymbol{E}^{\boldsymbol{3}} + \cdots \ \varepsilon_0 \chi^{(n)} \cdot \boldsymbol{E}^{\boldsymbol{n}} \tag{2}$$

where $\chi^{(1)}$ is the linear optical susceptibility, the same as in Eq. (1), and $\chi^{(2)}, \chi^{(3)}, \chi^{(n)}$ are nonlinear optical susceptibilities of second, third and n-order. In both cases, we are dealing with Lorentz model [12], for which electrons are bounded to the nucleus by a spring and oscillate harmonically upon external forces - electromagnetic radiation. What differentiates both regimes is the radiation intensity under which matter is subjected. When such interactions take place with intensities close to that of interatomic fields (approx. $10^8 \mathrm{V/cm}$), Eq. (1) stops describing accurately the light-matter interaction and cannot predict new phenomena.

These new phenomena are each correlated to some new $\chi^{(i)}$. For example, $\chi^{(2)}$ issues second harmonic generation (SHG), where two photons of same energy are 'combined' in a single one with double the initial energy, by interacting with the medium. The two most important nonlinear processes related to this work are the optical Kerr effect and two-photon absorption (TPA), both $\chi^{(3)}$ related processes. In order to examine these third-order nonlinear phenomena, we shall revisit and rearrange Eq. (2):

$$\boldsymbol{P} = \varepsilon_0\chi^{(1)}\boldsymbol{E} + \varepsilon_0\chi^{(3)}\boldsymbol{E^3} = \varepsilon_0\boldsymbol{E}\left(\chi^{(1)} + \chi^{(3)}\boldsymbol{E^2}\right) = \varepsilon_0\chi_{ef}\boldsymbol{E} \tag{3}$$

where we introduce an effective optical susceptibility:

$$\chi_{ef} = \chi^{(1)} + \chi^{(3)}I \tag{4}$$

where I denotes the electromagnetic field intensity. Now the refractive index takes form:

$$\tilde{n} = \sqrt{1 + \chi_{ef}} = \sqrt{1 + (\chi^{(1)} + \chi^{(3)}I)} \tag{5}$$

For low optical density mediums, $\tilde{n}$ can be expanded:

$$\tilde{n} \approx 1 + \tfrac{1}{2}\left(\chi^{(1)} + \chi^{(3)}I\right) = n + i\kappa \tag{7}$$

and by taking its real and imaginary parts:

$$n = 1 + \tfrac{1}{2}Re\left[\chi^{(1)}\right] + \tfrac{1}{2}Re\left[\chi^{(3)}\right]I = n_0 + n_2 I \tag{8}$$

$$\kappa = \tfrac{1}{2}Im\left[\chi^{(1)}\right] + \tfrac{1}{2}Im\left[\chi^{(3)}\right] \tag{9}$$

where n_0 is the linear refractive index, n_2 is the nonlinear refractive index related to $\chi^{(3)}$ and κ is proportional to the medium absorption α:

$$\alpha = \alpha_0 + \beta I \tag{10}$$

where α_0 is the linear absorption index and β is the nonlinear absorption index related to $\chi^{(3)}$.

Equations (8) and (10) show us how refraction and absorption of a medium can behave differently when subjected under intensities close to that of ionization. Moreover, they give us new ways of light-matter interaction. Equation (8) is responsible for the optical Kerr effect, which induces the self-focusing effect needed for the generation of ultrashort pulses on the Ti:sapphire laser, the most common laser system for fs-laser microfabrication and the one used in this work.

The Ti:sapphire laser, as well as several other lasers, presents a Gaussian transversal intensity profile, given by:

$$I(r) = I_0 e^{-\frac{r^2}{w^2}} \tag{11}$$

and the electromagnetic wave phase in the presence of the nonlinear refractive index can be written as:

$$\phi = \frac{2\pi n(I)}{\lambda} L = \frac{2\pi}{\lambda}(n_0 + n_2 I(r))L \tag{12}$$

so that the nonlinear phase becomes:

$$\Delta\phi = k n_2 I(r) L \tag{13}$$

Equation (13) gives us self-phase modulation. Due to the Gaussian aspect of the laser beam – intensity higher as closer to the center –, the material´s refractive index will be higher at the center than at the borders. This causes the wave propagation velocity to differ between center and border, effectively curving the wavefront. If the nonlinear refractive index n_2 is positive (as in Ti:sapphire crystals) the wavefront curvature acts by focusing the laser beam, while for negative n_2 the self-modulation acts by diverging the laser beam. The self-focusing importance for ultrashort pulse generation in Ti:sapphire laser will be discussed in the next section.

The last fundamental aspect of great importance in fs-laser micromachining is related to Eq. (10). Nonlinear absorption enables fs-laser micromachining to deterministically induce optical breakdown on transparent materials, as will be better discussed in Section 3.3.

3.2) Ultrashort pulses generation

Ultrashort laser pulses are characterized not only by its shortened duration ($10^{-12} - 10^{-15}$fs), but also by broadband optical spectrums and high peak intensity. They are generated by a process named as mode-locking, which can be induced via the optical Kerr effect; the whole process is called Kerr-lens-modelocking (KLM).

Ti:sapphire fs-lasers are systems with a sapphire crystal (Al_2O_3) doped with Ti^{3+}ions as active medium, which is excite by another laser operating in the range from 514 to $532\ nm$. In this work, a Nd:YVO$_4$ laser ($527\ nm$) was used. The Ti:sapphire crystal is placed inside a cavity, with prisms for dispersion control. The frequencies of the longitudinal cavity modes are given by:

$$\nu_m = m\frac{\mathrm{c}}{2L} \tag{14}$$

in which c is the speed of light, m an integer number and L is the cavity length. The cavity modes that will actually be excited depends on the laser gain medium spectral position and band, as seen in Figure 1. Ti:sapphire crystals presents a broad spectral band (up to $300\ nm$) centered at $800\ nm$.

As it can be seen in Figure 1, only the modes under the medium gain bandwidth will be amplified. Therefore, the resulting field can be written as:

$$E(t) = \sum_{m=1}^{N} E_m(t)\exp\left[i\left(2\pi\nu_m t + \phi_m(t)\right)\right] \tag{15}$$

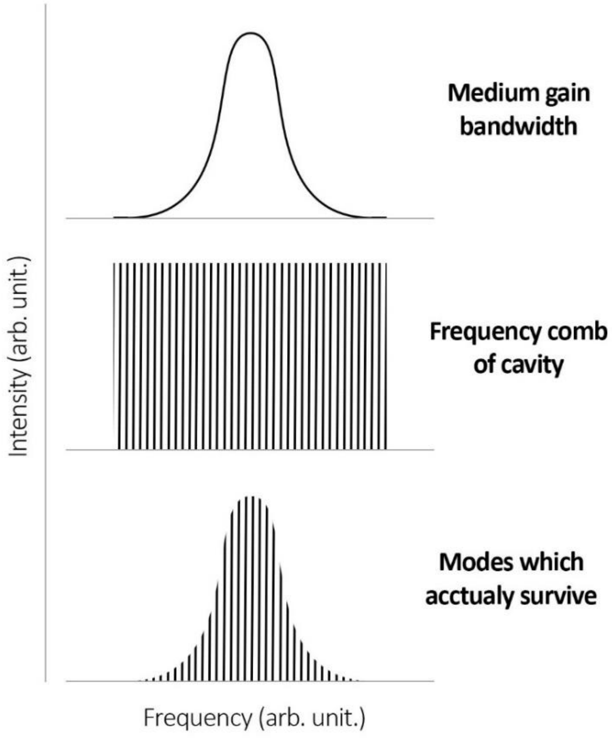

Figure 1: Schematic representation of which cavity allowed modes will be amplified by the medium

gain bandwidth.

From Eq. (15), it can be demonstrated that if the modes of the laser are locked in phase (mode-locking), ultra-short pulses can be generated by the constructive interference of the longitudinal modes. In Ti:sapphire lasers, modelocking is achieved by the KLM, which locks each mode in phase, since the laser cavity is designed to be more stable when the laser operates in the pulsed regime.

3.3) Ultrashort laser pulses interaction with transparent materials

Microfabrication via ultrashort laser pulses is due to laser-induced optical breakdown; that is, the laser energy deposited on the material excites a high number of electrons and ions, resulting in permanent phase or structural modification and also in material removal.

When processing transparent materials with ultrashort laser pulses, due to the high peak intensity achieved, excitation of the electrons from the valence band to the conduction band is initiated through nonlinear processes, such as multiphoton ionization Fig. 2. With ultrashort pulses of up to 10 fs, the energy is transferred to the electrons via nonlinear ionization [13;14] (Figure 3), while with longer pulses those nonlinearly excited electrons are further excited until they acquire enough kinetic energy to excite other bound electrons via collisions – a process called avalanche ionization [15].

It is in the first ~ 10 fs, when the electrons excitation begins, that multiphoton ionization plays an important role, supplying the first seed electrons to initiate avalanche ionization, which is the main responsible for increasing the density of excited electrons until they achieve plasma critic density. Once plasma is obtained, it linearly absorbs the laser light, leading to material damage. Although materials may have some seed electrons in the conduction band, resulting from impurities and defects, it is the multiphoton ionization mechanism that enables microfabrication via ultrashort laser pulses to occur deterministically and independently of the material.

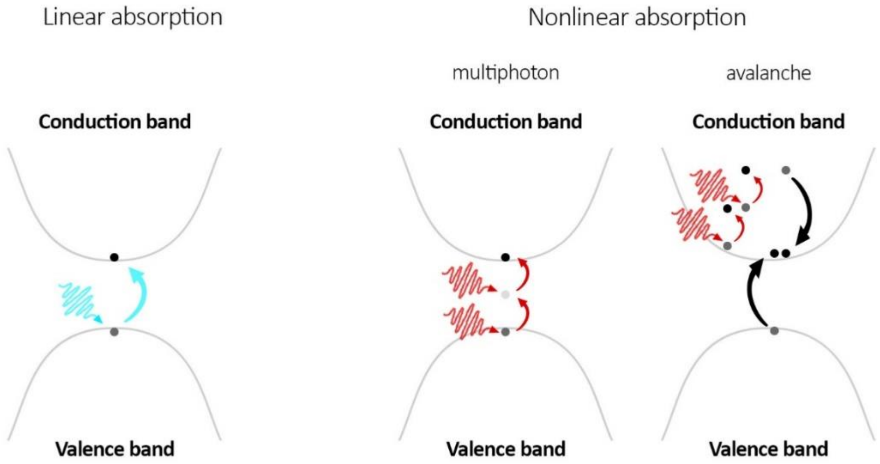

Figure 2: Representation of linear and nonlinear absorption processes at femtosecond timescale.

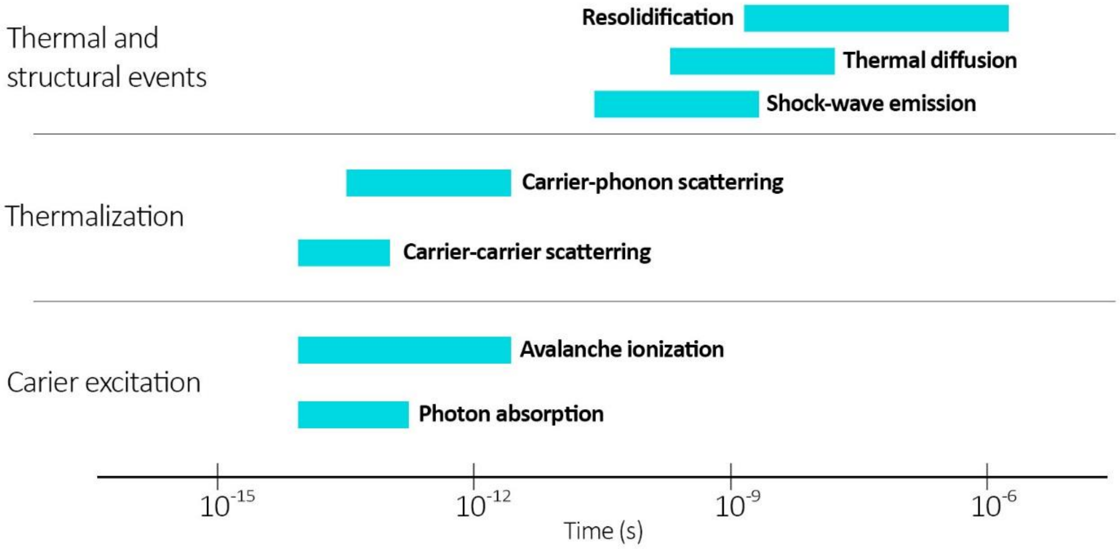

Figure 3: Timescale of the physical phenomena associated with ultrashort pulses interaction with transparent materials. Cyan bars represent typical timescale for each process.

From Fig. 3 we see that the laser to lattice energy deposition process starts and finishes before the thermal regime, so that very little heat is distributed out of focal volume, enabling micro and nano resolution features to be fabricated. Moreover, it allows microfabrication on delicate materials such as biological tissues, with almost no heat-affected zones (HAZ) [16].

Material´s phase and structural modification, as well as ablation can be induced and controlled three-dimensionally on the transparent material volume, since only at the focal volume the ultrashort pulse can achieve high enough intensity for the nonlinear ionization to occur. Ablation is caused mainly by Coulomb repulsion, due to the large accumulation of positive charges (ionized atoms) after pulse arrival. With high density of excited electrons, spatially separated from the ions fixed in the lattice, the Coulomb repulsion energy achieves values higher than the bounding energy of the crystalline network, deforming it structurally and ejecting material, a process called Coulomb explosion. Finally, pulse energy and repetition rate will influence directly the features of induced structures. Single low energy pulses may not induce optical breakdown, requiring a high repetition rate (MHz) to, by a cumulative regime, gather enough energy inside and around the focal volume, leading to optical breakdown.

3.4) Surface Wetting models

Surface´s wettability can be changed by modifying its roughness [17], [18] and, therefore, understanding such a process is crucial for many applications. The surface roughness can make the apparent contact angle measured different from those obtained in the flat (non roughened surface). Different models have been used to describe the wetting of rough/textured surfaces [19]–[21] (Fig.

4). The Wenzel model [20] describes the homogeneous wetting regime. In this model, surface roughness r, defined as the ratio of the actual surface in contact with the liquid to its projection, always magnifies the wetting properties, either hydrophilic or hydrophobic. In this case the apparent contact angle θ^* is given by

$$\cos\theta^* = r\cos\theta \tag{16}$$

in which θ is the contact angle measured on the flat surface.

The Cassie model [19], on the other hand, describes the wetting of a heterogeneous surface. For the case in which air can be trapped on a rough surface, such that the liquid does not completely wet the solid, the so-called Cassie-Baxter model applies. In such case, the contact angle of the roughened surface θ^* is given by

$$\cos\theta^* = f(\cos\theta + 1) - 1 \tag{17}$$

where f is the fraction of solid underneath the drop and θ is the contact angle for the flat surface. In this case, which leads to an increase in the hydrophobicity; the smaller the value of f the larger is the increase in the measured contact angle [21].

Although the Cassie-Baxter and Wenzel models have been successfully used to explain a large number of the observed wetting behavior, there is still one wetting regime, namely the Cassie-impregnating wetting model. For such wetting regime, one considers that pores are filled with liquid and solid "islands" ahead the drop are dry [22], [23], i.e., the drop lies on a solid/liquid composite surface, and a liquid film impregnates the solid texture ahead the drop. The apparent contact angle for the Cassie-impregnating state is given by

$$\cos\theta^* = f(\cos\theta - 1) + 1 \tag{18}$$

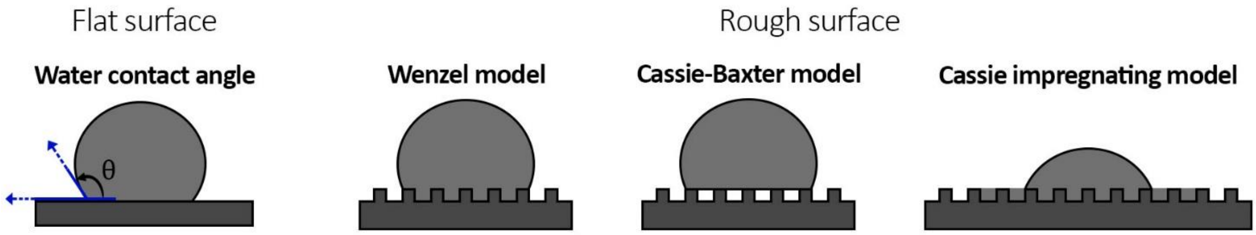

Figure 4: Wetting regimes on flat and rough surfaces.

4) Experimental

4.1) TFEMA-DR13 films

The TFEMA-DR13 films were synthesized by radical polymerization as described in Ref. [1]. The reaction was conducted in a solution of 4 mL of methyl-ethyl-ketone (MEK) and dimethylformamide (DMF) (3:1, v/v), with 0.015 g of AIBN as thermal initiator and 30% in mass of the azomonomer in relation to the fluoridated one. The temperature during synthesis was 70 ^{o}C. Films of the copolymer were then cast from 5 g/L solutions in chloroform onto glass slides at 40 ^{o}C and maintained at this temperature until complete evaporation of the solvent. UV-Vis absorption spectroscopy was performed in the TFEMA-DR13 film using a Shimadzu UV-1800® spectrophotometer. To determine the surface wettability of the copolymer, contact angle measurements were performed using a KSV CAM 200 goniometer.

4.2) Fs-laser micromachining setup

The TFEMA-DR13 was microstructured using a femtosecond laser oscillator (Femtosource XL) delivering 50-fs pulses centered at 800nm, with a repetition rate of 5 MHz. The surface modification was carried out by focusing the femtosecond laser pulses onto the surface sample with the aid of a microscope objective (0.65NA). The sample was positioned on a x-y-z translational stage, moving at constant speed, allowing the microfabrication of arbitrary geometries onto the TFEMA-DR13 surface. A diagram of the micromachining setup is displayed in Fig. 5.

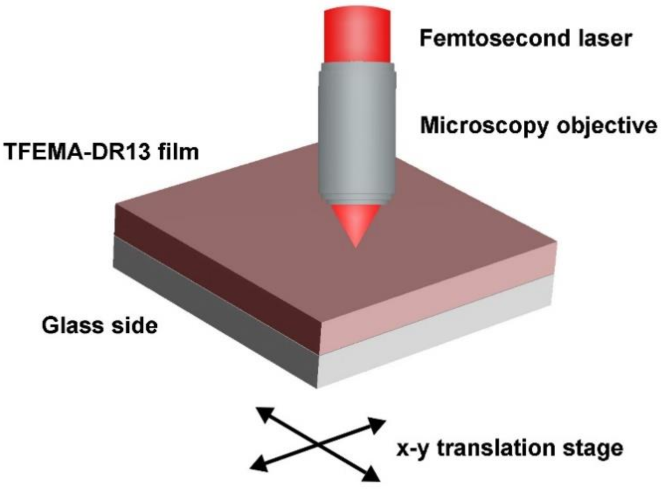

Figure 5: Femtosecond laser micromachining experimental setup.

Each translation stage is attached by a stepper motor, which is controlled by a LabVIEW program developed by our group. The whole process was also real-time monitored using a CCD camera, aligned to the microscope objective. The laser pulse energy and translation speed were varied in order to obtain optimal irradiation conditions for microfabrication.

Femtosecond-laser micromachining of the copolymer surface was analyzed by optical microscopy (Zeiss LSM 700) and by scanning electron microscopy (SEM) using a Tabletop Microscope (TM3000).

5) Results

5.1) TFEMA-DR13 linear absorption

To benefit from one of the greatest achievements of ultrashort pulses, minimal heat-affected zone surrounding the laser spot region, the laser beam must not be linearly absorbed by the material. With this regard, UV-Vis absorption spectroscopy was performed on the TFEMA-DR13 film, using a Shimadzu UV-1800® spectrophotometer. The absorption spectrum, displayed in Fig. 6, presents an absorption band centered at 477 nm, corresponding to the π→π* electronic transition of the azochromophore DR13[25].

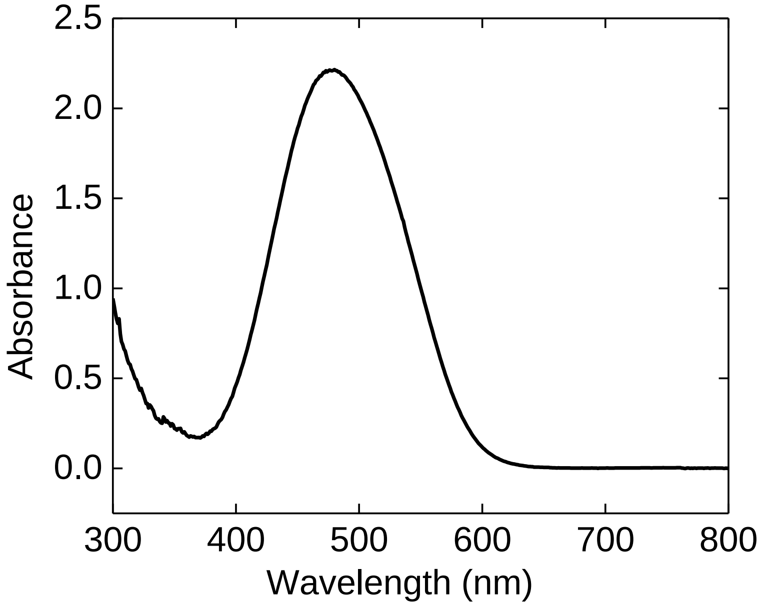

Figure 6: UV-Vis absorption spectrum of TFEMA-DR13.

5.3) TFEMA-DR13 material removal threshold energy

In order to study the microfabrication conditions on the TFEMA-DR13, ablated lines were structured onto the copolymer surface for characterization of the minimum energy for material removal by the Zero Damage Method (ZDM) [26]. Several groups of four lines were inscribed onto the copolymer surface, 20 μm apart, with pulse energy varying from one group to another, but with constant scanning speed. First from 10 nJ to 16 nJ, for 50 μm/s, and then repeated for scanning speed of 100 μm/s from 14 nJ to 20 nJ. The lines were then analyzed by optical microscopy (Fig. 7) and by scanning electron microscopy (Fig. 8).

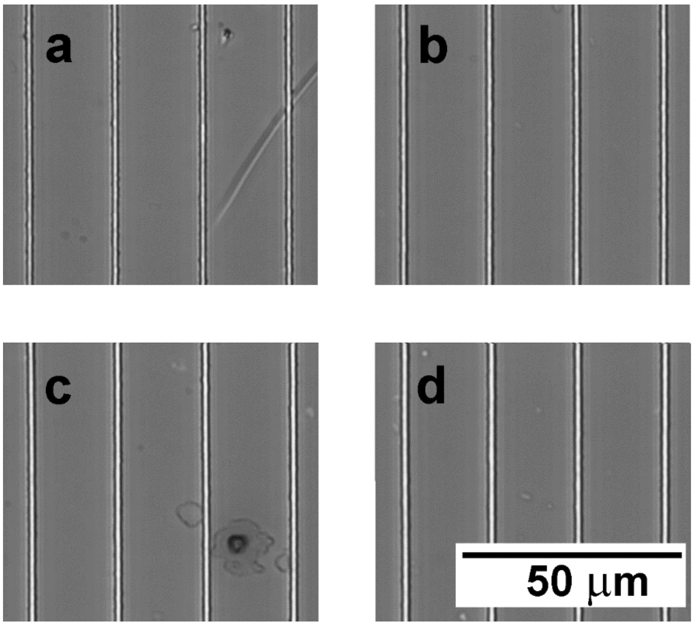

Figure 7: Optical microscopy images of femtosecond TFEMA-DR13 micromachined lines, using a) 14 nJ; b) 16 nJ; c) 18 nJ; d) 20 nJ of pulse energy for 50 μm/s of translation speed. The bright regions correspond to the laser-ablated material.

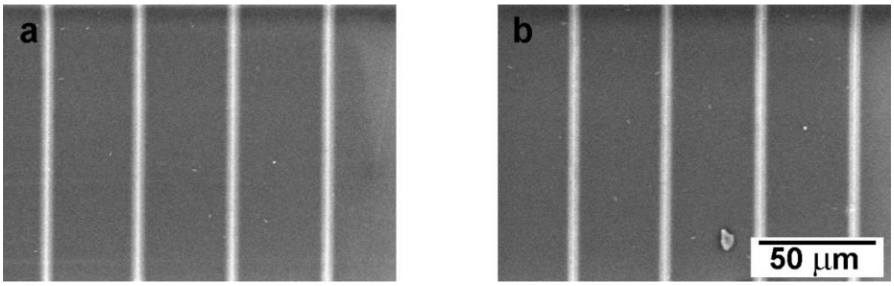

Figure 8: Scanning electron microscopy images of femtosecond TFEMA-DR13 micromachined lines with scanning speed of 100 μm/s and with pulse energy of a) 14 nJ and b) 18 nJ.

It is noted that the lines present a continuous character and a high uniformity at the higher pulse energies, suggesting good optical quality. From optical microscopy images of all groups microfabricated, we were able to measure and average each of the four lines widths, determining a line width for each group, which were then plotted as a function of the pulse energy, according to:

$$W^2(r) = \frac{W^2{}_0}{2} ln\left(\frac{E}{E_{th}}\right) \qquad [19]$$

in which the radius width is denoted as W. W_o is the beam waist, and E is the pulse energy, with E_{th} being the material removal threshold. Each group of lines corresponds to one point on the graph in

Fig. 9.

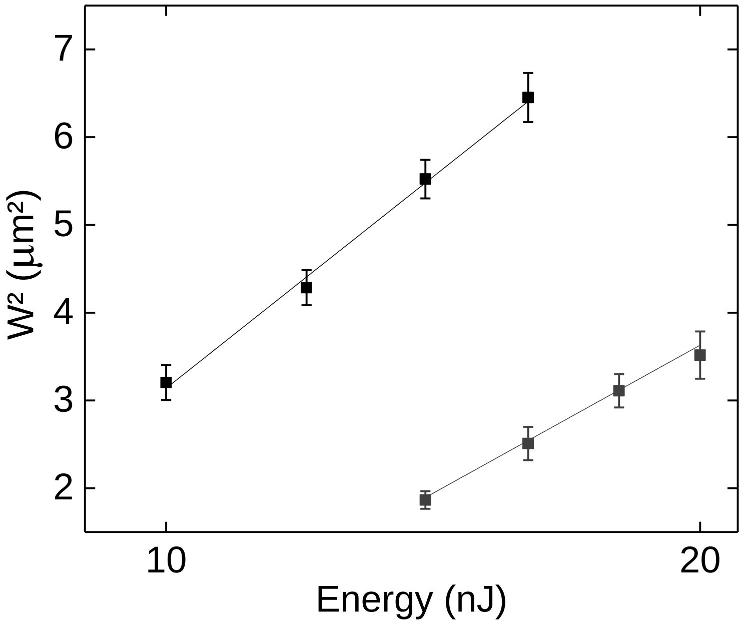

Figure 9: Squared line width as a function of the pulse energy using 50 μm/s (points in black) and 100 μm/s (points in grey) of translation speed.

As we can see in Fig. 9, the squared average line width increases well according to the ZDM model as the pulse energy increases. For scanning velocity of 50 μm/s, the line width starts at 1.8 μm for 10 nJ and rises to 2.5 μm for 16 nJ, while for 100 μm/s, the line width starts at 0.5 μm for 14 nJ and rise up to 1.7 μm for 20 nJ of pulse energy. Fitting this data using Eq. (19), the threshold energy for material removal could be determined, with values of 3.2 nJ and 5.1 nJ, for 50 μm/s and 100 μm/s, respectively. The difference between the two threshold energies is due to the cumulative behavior of the micromachining process. Because of the high repetition rate of the fs-laser oscillator used, on the order of MHz, and pulse energies on the order of nJ, the pulses are separated by a time much shorter than the characteristic time for heat diffusion. When the sample is perpendicularly translated, a different number of pulses strikes the copolymer at each velocity. At lower translational speed, more pulses arrive damaging the sample surface, hence a lower energy threshold.

Atomic force microscopy was performed on ablated lines microfabricated with the aid of 3 different microscope objectives (10x; 20x; 40x), in a range of pulse energy varying from 12 nJ up to 20 nJ, for 50 μm/s of sample scanning speed. According to the optical microscopy images, higher energies produced more uniform and continuous lines (Fig. 7), whereas the microscope objective with 40x amplification (0.65 NA) produced the cleanest ablated lines. In Fig. 10 d), it is seen the optimal conditions achieved, with 16 nJ of pulse energy, 50 μm/s of sample scanning speed, and a 40x (0.65 NA) microscope objective. The total depth of material removal is 500 nm with 2.54 μm width at surface level.

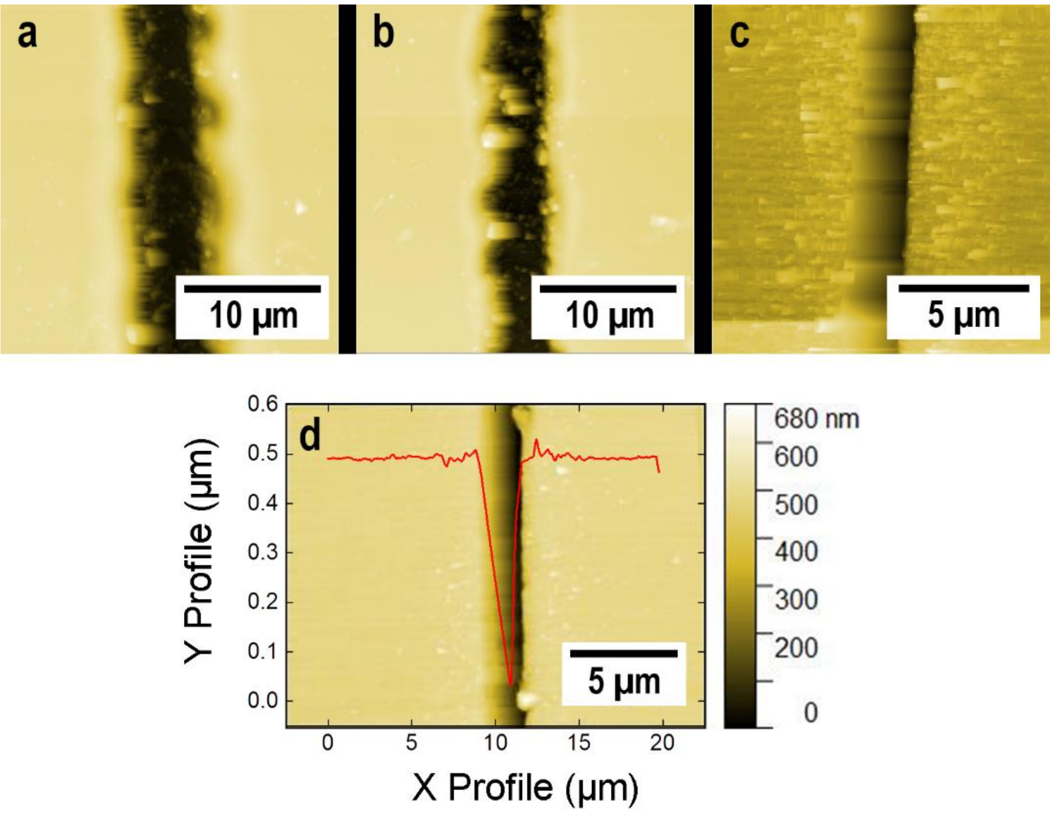

Figure 10: Atomic force microscopy images of ablated lines microfabricated with 20 nJ pulse energy, 50 µm/s of scanning speed and with the aid of an objective with amplification of a) 10x; b) 20x; c) 40x. And d) with 16 nJ, 50 µm/s, 40x, alongside profile graph.

5.4) Periodic surface patterning

With the optimal conditions established for the femtosecond-laser microfabrication, a pattern composed of micropillars with squared cross-section was chosen, due to its previous success in wettability control [27], and microfabricated onto TFEMA-DR13 surface. By varying the cross-sectional area of the micropillars in each set, the roughness factor (or roughness area ratio) varies as described by Wenzel, and the water contact angle should vary as well, indicating a wettability improvement or worsening.

The TFEMA-DR13 surface was microstructured with four sets of micropillars, each disposed in an area of 1 mm². The cross-sectional area was varied as the pattern periodicity changed in each set: 20, 30, 40 and 50 µm. The microstructured surface was then analyzed by scanning electron microscopy (Figure 11), where the ablated lines uniformity and continuity were attested.

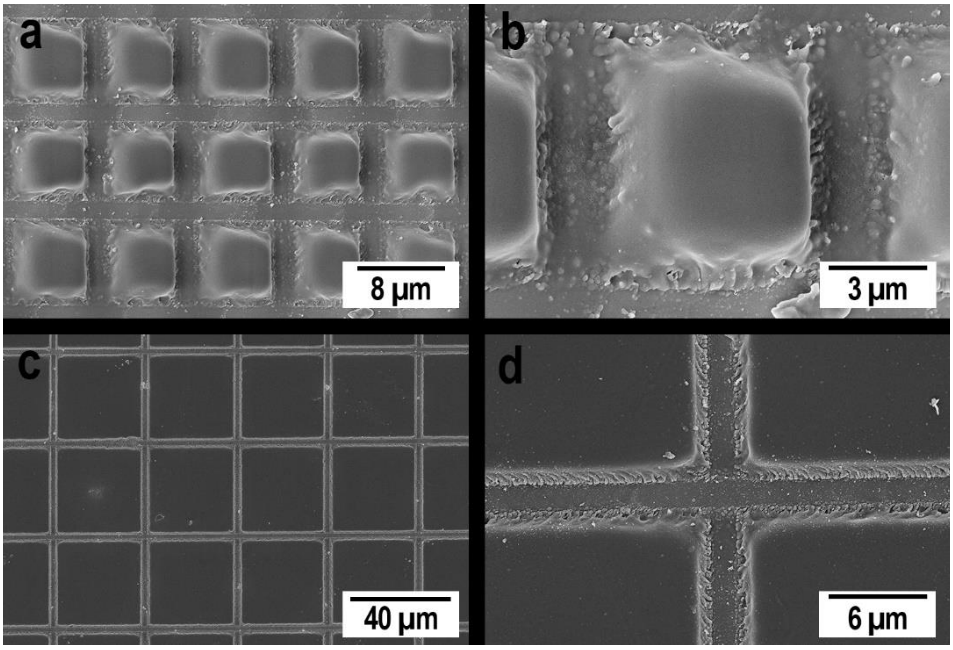

Figure 11: Scanning electron microscopy of TFEMA-DR13 microstructured with periodicity of a) and b) 10 µm; c) and d) 40 µm.

5.5) Contact angle on microstructured TFEMA DR13

The contact angle between a water droplet (2 µl) and the TFEMA-DR13 unstructured surface was measured using a goniometer. As presented in Fig. 11, the unstructured copolymer surface presents a partial wetting regime, with a contact angle of (89.6 ± 0.3)°.

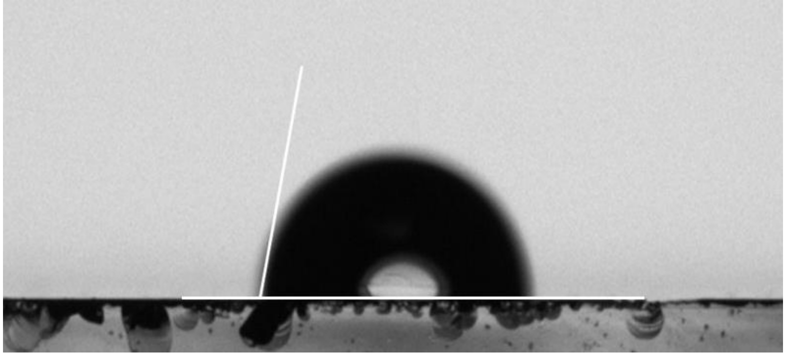

Figure 12: Image of a water droplet on the unstructured surface of TFEMA-DR13

Figure 13 shows some contact angle measurements for the structured TFEMA-DR13 with a water droplet of 2 µl.

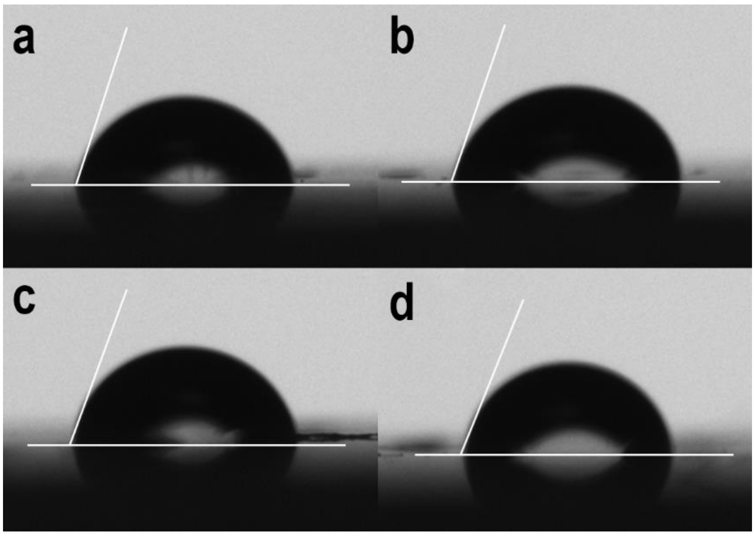

Figure 13: Goniometer measurement images of water contact angles in the microstructured surface of TFEMA-DR13 with periodicity a) 50 μm with 82.7°; b) 40 μm with 80.8°; c) 30 μm with 78.2°; d) 20 μm with 74.1°.

Figure 14 (black circles) displays the experimentally determined apparent contact angle, θ^*, obtained as a function of f for the corresponding surface patterns with different periodicities (indicated in the top axis). A clear decrease in contact angle is observed, 15.5°, denoting an improvement on the wettability feature of the sample and highlighting the hydrophilic behavior of the TFEMA-DR13 surface, which was ambiguous as the contact angle on the unstructured surface (89.6 ± 0.3)° laid in the halfway between hydrophilicity and hydrophobicity regime.

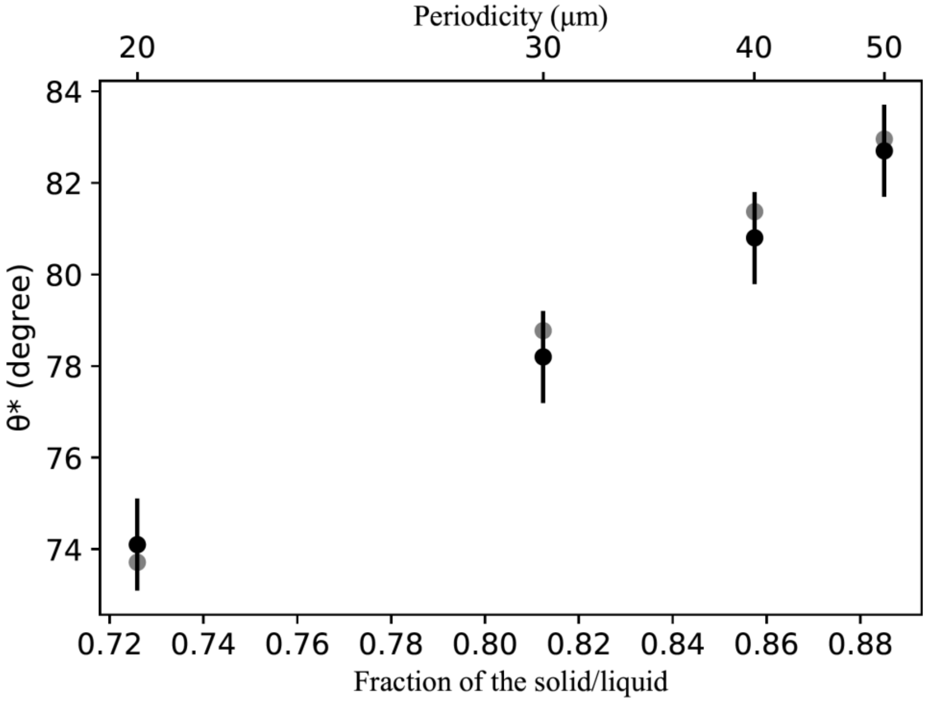

Figure 14: The black circles represents the apparent contact angle for water measured on the

microstructured surfaces as a function of the fraction of the solid/liquid (lower axis) and the periodicity of the surface pattern (upper axis). The grey circles represent the values obtained using the Cassie-impregnating state.

By applying the Wenzel model (Eq. (16)) to the microstructured surface with a period of 20 μm, which corresponds to r = 1.07, one obtain an apparent contact angle of θ^*= 89.4°, which is very close to the one observed for the unstructured surface and, therefore, higher than the value experimentally observed (θ^*= 74.1± 0.9°). Such a result indicates that the Wenzel's model does not describe the experimental data and, therefore, the produced samples are not in the homogeneous wetting regime. As mentioned before, the grey circles in Fig. 13 correspond to the values obtained using the Cassie-impregnating model. As one can see, the experimental data are in excellent agreement with the Cassie-impregnating model, indicating a state where the microscopic cavities are partially filled with a liquid underneath the droplet.

6) Conclusion

In conclusion, we have demonstrated the microfabrication via femtosecond laser of the TFEMA-DR13 copolymer surface, determining the experimental conditions for the ablation regime; material removal energy threshold (3.2 nJ for 50 μm/s and 5.1 nJ for 100 μm/s). We have also determined the surface wettability of the unstructured copolymer sample (89.6°) and the optimal conditions for surface patterning are: 16 nJ of pulse energy; 40x 0.65NA microscope objective; 50 μm/s of sample translational speed. With these conditions, four sets of squared-shaped micro pillars were microfabricated. The water contact angle measured revealed a difference of 15.5° between the sets with higher roughness factor and the unstructured sample. The dependence of the contact angle with the surface morphology is in agreement with the Cassie-impregnating wetting model, indicating a state where the microscopic cavities are partially filled with a liquid underneath the liquid droplet.

7) References

[1] R. C. Sanfelice, F. J. Pavinatto, M. R. Cardoso, C. R. Mendona, D. T. Balogh, and O. N. Oliveira, "Hydrophobic methacrylic copolymers containing azobenzene moieties," *Polymer (Guildf).*, vol. 52, no. 21, pp. 4703–4708, 2011.

[2] K Guan, "Relationship between photocatalytic activity hydrophilicity and self-cleaning effect of TiO2/SiO2 films," *Surf. Coatings Technol.*, vol. 191, no. 2—3, pp. 155-160, 2005.

[3] S. Nishimoto and B. Bhushan, "Bioinspired self-cleaning surfaces with superhydrophobicity, superoleophobycity, and superhydrophilicity," *RSC Adv.*, vol. 3, no. 3, pp. 671—690, 2013.

[4] R. L. McCarley, S. A. Soper, M. C. Murphy, S. Y. Wei, A. F. Smith, B. Vaidya, and J. Feng,

“Resist-Free Patterning of Surface Architectures in Polymer-Based Microanalytical Devices,” *Micro Total Anal. Syst. 2004, Vol 2*, no. 297, pp. 130–132, 2005.

[5] Y. SH, L. YS, L. FH, Y. JM, and C. KS, “An Improved Hydrophilicity via Electrospinning for Enhanced Cell Attachment and Profliferation,” *J. Biomed. Mater. Res. B. Appl. Biomater.*, vol. 83, no. 2, pp. 340—344, 2007.

[6] M. O. Klein, A. Bijelic, T. Toyoshima, H. Götz, R. L. von Koppenfels, B. Al-Nawas, and H. Duschner, “Long-term response of osteogenic cells on micron and submicron-scale-structured hydrophilic titanium surfaces: Sequence of cell proliferation and cell differentiation,” *Clin. Oral Implants Res.*, vol. 21, no. 6, pp. 642–649, 2010.

[7] A. Nakajima, K. Hashimoto, T. Watanabe, “Recente studies on super-hydrophobic films,” *Monatsh Chem.*, vol 132, pp. 31—41, 2001

[8] Z. Gao, J. Sun, S. Peng, L. Yao, and Y. Qiu, “Surface modification of a polyamide 6 film by He/CF 4 plasma using atmospheric pressure plasma jet,” *Appl. Surf. Sci.*, vol. 256, no. 5, pp. 1496–1501, 2009.

[9] and A. J. P. A.R. Postema, A.T. Doornkamp, J.G. Meijer, H.v.d. Vlekkert, “Effect of chlorosulfonation of ultra-high strength polyethylene fibres on mechanical properties and bonding with gypsum plaster,” *Polym. Bull.*, vol. 16, pp. 1–6, 1986.

[10] M. Ma, Y. Mao, M. Gupta, K. K. Gleason, and G. C. Rutledge, “Superhydrophobic fabrics produced by electrospinning and chemical vapor deposition,” *Macromolecules*, vol. 38, no. 23, pp. 9742–9748, 2005.

[11] K. T. Paula, G. Gaál, G. F. B. Almeida, M. B. Andrade, M. H. M. Facure, D. S. Correa, A. Riul, V. Rodrigues, and C. R. Mendonça, “Femtosecond laser micromachining of polylactic acid/graphene composites for designing interdigitated microelectrodes for sensor applications,” *Opt. Laser Technol.*, vol. 101, pp. 74—79, 2018.

[12] M. Sheik-Bahae, A. A. Said, T. Wei, D. Hagan and E. W. Van Stryland, IEEE J. Quantum Eletronics. **QE-26**, 760 (1990).

[13] Stuart, B. C., Feit, M. D., Rubenchik, A. M., Shore, B. W. & Perry, M. D. Laser-induced damage in dielectrics with nanosecond to subpicosecond pulses. Phys. Rev. Lett. 74, 2248–2251 (1995).

[14] Stuart, B. C. et al. Nanosecond-to-femtosecond laser-induced breakdown in dielectrics. Phys. Rev. B 53, 1749–1761 (1996).

[15] Bloembergen, N. Laser-induced electric breakdown in solids. IEEE J. Sel. Top. Quant. Electron. 10, 375–386 (1974).

[16] Srinivasan R, Sutcliffe E, Braren B. Ablation and etching of polymethylmethacrylate by very short (160 fs) ultraviolet (308 nm) laser pulses. Appl Phys Lett 1987.

[17] K. J. Kubiak, M. C. T. Wilson, T. G. Mathia, and P. Carval, “Wettability versus roughness of engineering surfaces,” *Wear*, vol. 271, no. 3–4, pp. 523–528, 2011, doi: 10.1016/j.wear.2010.03.029.

[18] Hideo Nakae, Ryuichi Inui, Yosuke Hirata, and Hiroyuki Saito, “Effects of surface roughness on wettability,” *Acta Mater.*, vol. 46, no. 7, pp. 2313–2318, 1998, doi: 10.1016/s1359-6454(98)80012-8.

[19] A. B. D. Cassie, “Contact Angels,” *Discuss. Faraday Soc.*, vol. 3, pp. 11–16, 1948.

[20] R. N. Wenzel, “Resistance of solid surfaces to wetting by water,” *Ind. Eng. Chem.*, vol. 28, no. 8, pp. 988–994, 1936, doi: 10.1021/ie50320a024.

[21] B. D. Cassie, “Of porous surfaces,” no. 5, pp. 546–551, 1944.

[22] E. Bormashenko *et al.*, “Characterization of rough surfaces with vibrated drops,” *Phys. Chem. Chem. Phys.*, vol. 10, no. 27, pp. 4056–4061, 2008, doi: 10.1039/b800091c.

[23] P.-G. de Gennes, F. Brochard-Wyart, D. Quéré, P.-G. de Gennes, F. Brochard-Wyart, and D. Quéré, *Special Interfaces*. 2004.

[24] H. S. Silva, F. J. S. Lopes, and P. B. Miranda, “Molecular ordering of PAH/MA-co-DR13 azopolymer layer-by-layer films probed by second-harmonic generation,” *J. Chem. Phys.*, vol. 145, no. 10, 2016.

[25] J. M. LIU, “Simple technique for measurements of pulsed Gaussian-beam spot sizes,” *Opt. Lett.*, vol. 7, no. 5, pp. 196–198, 1982.

[26] Cardoso, Marcos R., et al. "Highly hydrophobic hierarchical nanomicro roughness polymer surface created by stamping and laser micromachining." *Journal of Applied Polymer Science* 132.24 (2015).